Observations of Near-Inertial Waves in a Front

ERIC KUNZE AND THOMAS B. SANFORD

Applied Physics Laboratory and School of Oceanography, University of Washington, Seattle, WA 98105

(Manuscript received 16 June 1983, in final form 26 October 1983)

ABSTRACT

Near-inertial motions with horizontal scales ~O(10 km) dominate profiles of velocity finestructure collected in the North Pacific Subtropical Front during January 1980. Considerable spatial variability is observed. Two features in particular contain most of the energy: a 20 cm s^{-1} amplitude (λ_z = 100 m) wave on the warm edge of the front propagating downward and away from the front, and a low wavenumber (λ_z = 500 m) wave reflecting off the surface. The propagating wavegroup is four times as energetic as the local downgoing near-inertial wave field. Its spatial structure is not consistent with propagation in a homogeneous medium, which suggests that it may be interacting with the front. Possible mechanisms for the existence and properties of the wavegroup are discussed, including baroclinic/barotropic instability, wind-forcing and enhancement by wave-mean flow interaction. A wave–mean flow interaction model that predicts trapping and amplification of near-inertial waves in regions of negative vorticity reproduces the observed features most consistently.

1. Introduction

The influence of low-frequency shear on the ubiquitous internal wave field has received much attention over the past decade. Müller (1976) parameterized the interaction in terms of eddy viscosities by assuming the equilibrium internal wave state was the same in shear as in the unsheared ocean. Using the Garrett and Munk (1972, 1975) canonical spectrum, he estimated vertical and horizontal eddy viscosities of $\nu_z \sim 0.4$ m^2 s^{-1} and $\nu_H \sim 7$ m^2 s^{-1}. But observations have shown that the vertical viscosities induced by internal waves in shear are at least an order of magnitude smaller than Müller's calculated values (Frankignoul and Joyce, 1979). Ruddick and Joyce (1979) indicated that the internal wave field could relax to a different equilibrium state in shear, and so reduce the momentum exchange. McComas and Bretherton (1977) argue that Müller greatly overestimated the relaxation time and, therefore, the eddy viscosities. On the other hand, horizontal viscosities observed at the LDE site (Brown and Owens, 1982) were 100 m^2 s^{-1}, larger than Müller's estimates. It should be pointed out that because Müller's mechanism excludes critical layers he found a negligible contribution from the critical-layer prone near-inertial waves.

Near-inertial motions have been observed to be strongly modulated by geostrophic shear. Fu (1981) reported enhanced near-inertial motions under the Gulf Stream, and Frankignoul's (1976) figures show intense near-inertial motion when the low-frequency vorticity is negative. Time-series of near-inertial energy and low-frequency shear often look similar (see, e.g., Frankignoul and Joyce, 1979; Brown and Owens, 1982; Hayes, 1979). Ruddick and Joyce (1979) point out that time series of low-frequency shear and total internal wave energy (dominantly near-inertial) have similar behavior, suggesting interaction between geostrophic shear and near-inertial waves; yet they assumed near-inertial motions did not contribute to the interaction when calculating their eddy viscosities.

The mechanisms responsible for this correlation are not clear. Plausible candidates are: i) generation during geostrophic adjustment after, e.g., instability of the flow, and ii) interaction with the mean flow.

Ageostrophic flow, imparted by wind-forcing or instability, will generate near-inertial waves while undergoing geostrophic adjustment (Rossby, 1938). Up to 0.8 of the unbalanced energy will go into near-inertial motions if the forcing variability is on timescales < O(1 day) (Veronis, 1956); for longer timescales, less energy is taken up by the waves and more by the geostrophic flow. Quasi-geostrophic variability has been observed on timescales < 3–4 days in the North Atlantic convergence zone (Leetmaa and Voorhis, 1978) and <7 days in the North Pacific Subtropical Front (Roden, 1981), with the actual timescales unresolved in both cases. Tang (1979) found intense near-inertial motions associated with the veering of low-frequency currents in the Gulf of St. Lawrence. Csanady (1978) reported inertial oscillations associated with the movement of a front in Lake Ontario, but this movement was forced by winds, so it is not clear that the waves weren't wind-generated.

It has been reported that vorticity perturbs the limiting frequency of near-inertial waves (Perkins, 1976; Weller, 1982). In the presence of geostrophic vorticity ζ, the planetary value of the Coriolis frequency f is shifted to an effective Coriolis frequency $f_{\text{eff}} \approx f + \zeta/2$. This has broad implications for near-inertial waves

propagating in a field of horizontally and vertically nonuniform vorticity. Since the effective Coriolis frequency is the lower bound of the internal waveband, near-inertial waves should be trapped in regions of negative vorticity where the effective Coriolis frequency is reduced. In negative vorticity, near-inertial waves (where near-inertial is taken to mean near the *effective* Coriolis frequency) have intrinsic frequencies below the effective Coriolis frequency of the surrounding ocean, so cannot propagate out of the region.

The influence of mean-flow shear on near-inertial waves will be explored in this paper, using observations of the internal wave velocity field collected in the North Pacific Subtropical Front during the FRONTS '80 experiment (Niiler, 1982; EOS Transactions, 1980). The measurements were made with the expendable current profiler (XCP) (Drever and Sanford, 1980). Most internal wave studies have been based on current meter data that emphasize the statistical properties of internal waves in the frequency domain. In contrast, here several horizontal sections of velocity profiles across the front are presented. These sections represent an almost instantaneous snapshot of the spatial structure of the energetic near-inertial field. Adjacent profiles were coherent for these waves.

In this dataset, individual wavegroups can be distinguished. From their vertical scales and horizontal phase behavior, estimates of frequency and group velocity are obtained. Two energetic features are observed in the data, both in the near-inertial field:

1) an isolated, downward-propagating wavegroup on the warm edge (negative vorticity side) of the front with four times as much energy as the background internal wave level, and

2) a low-wavenumber vertically stationary wave within the front that has a vertical wavelength of 500 m.

The horizontal scales of both these features are ~O(10 km), a scale similar to the width of the front. These waves contain a large fraction of the energy in the internal wave field and are energetic enough to play an important role in the front's dynamics. Possible interaction with the mean flow field is investigated with a ray-tracing theory.

2. The mesoscale features of the front

The North Pacific Subtropical Front is a permanent feature, extending across the entire basin at ~30°N (Fig. 1 after Roden, 1975). The front is evident in both temperature and salinity fields, with horizontal gradients strongest in the upper few hundred meters. It is believed to be controlled by the latitudinal distribution of wind stress and solar heat flux (Roden and Paskausky, 1978).

The FRONTS '80 experiment took place during January 1980, 1000 km north of Hawaii (the box in Fig. 1) in water depths of 6000 m, well away from any coast or bottom topography that might perturb the quasi-geostrophic, tidal, or internal wave flow fields. It was a multi-investigator endeavor to improve our understanding of the dynamics of open ocean fronts. Measurements were made on scales ranging from hundreds of kilometers to turbulent dissipation scales of centimeters using both shipboard and satellite instrumentation.

The front was convoluted at the time of the experiment with a zonal "wavelength" of 200 km and a peak-to-trough amplitude of 100 km, consistent with long-term satellite observations (Sowinsky and Green, personal communication, 1982; Van Woert, 1982). Fig. 2a shows the experimental site, roughly 180 × 180 km. The contours are of density, averaged over 180–300 m, from Roden's (1981) CTD survey of 24–30 January 1980. Although the CTD survey was taken

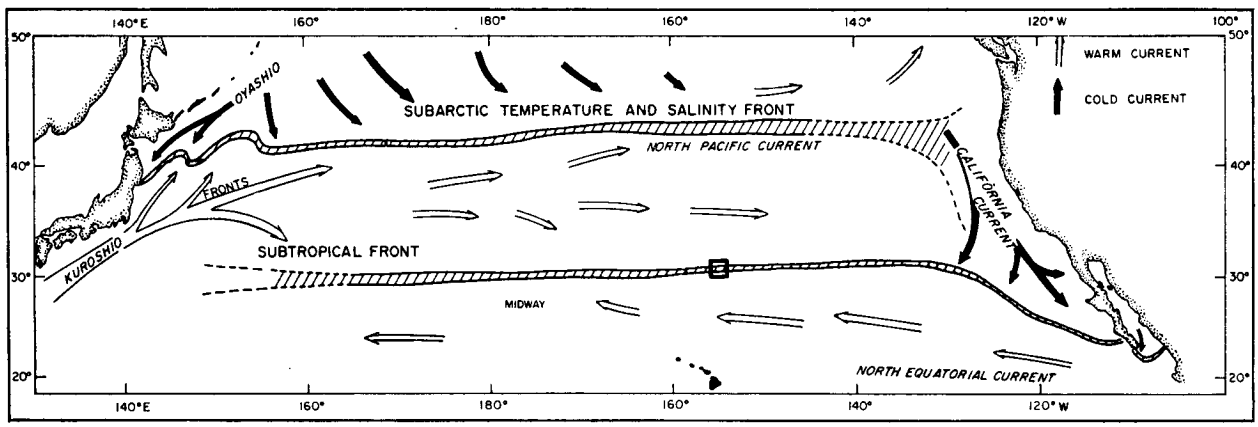

FIG. 1. Schematic of midlatitude fronts of the North Pacific (after Roden, 1975). The North Pacific Subtropical Front extends across the entire basin at ~30°N. The FRONTS '80 experiment took place in the area indicated by the box at 153°W, 1000 km north of Hawaii.

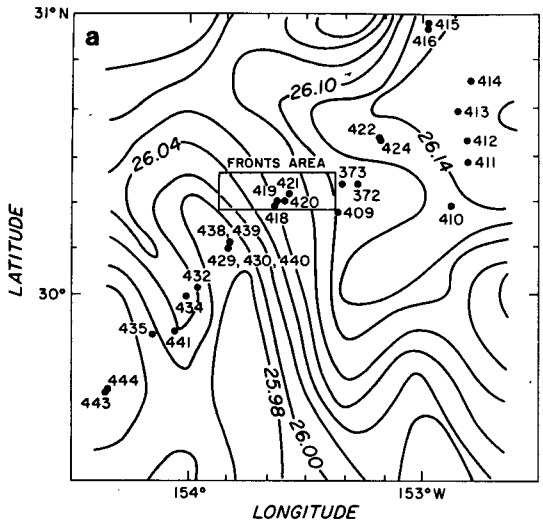

FIG. 2a. The FRONTS '80 experimental site. Contours are of sigma-t averaged over 180–300 m (Roden, 1981). The positions of the XCP drops are indicated by the FRONTS area inset (see Fig. 2b) and the numbered dots.

one week after the XCP measurements, changes in the front were small, so these contours represent the configuration of the front during the XCP measurements.

The 37 km spacing between CTD casts does not permit resolution of the front width, which is better seen in the more closely-spaced XBT sections. Sections were made across the front on 19, 21, and 25 January. In Fig. 3, XBT temperatures (averaged over 180–300 m to reduce high wavenumber noise) are plotted across the front. The stippling envelops 95% of the observed values. On 19 January the temperature front is well defined as a temperature jump of 1°C, corresponding to a σ_t jump of 0.16‰, over 20 km between 153°35′ and 50′W. The T, S relation did not change across the front; i.e., the front was noncompensating, allowing density to be estimated from temperature alone. Comparison with the later XBT sections on 21 and 25 January, which corresponded to the XCP sections, reveals that the lateral position of the front did not change significantly, consistent with acrossfront movement of less than 2 cm s^{-1}. The spatially-averaged temperature gradient did not change during this period. The scatter seen on 21 and 25 January is within the maximum error of 0.3°C specified by the manufacturer (Sippican), and is a factor of 2 larger than what would be expected from internal wave displacements based on the Garrett and Munk spectrum (Munk, 1981).

Associated with the front is a surface geostrophic jet with maximum southward velocities of 20 cm s^{-1} in the 120-m thick mixed layer. The jet decays rapidly in the upper pycnocline, with an exponential decay scale of ~100 m. Table 1 compares the surface jet's magnitude, position and width as deduced from CTD (Roden, 1981) and XBT measurements (providing estimates of the geostrophic flow), direct measurements of the flow by satellite-tracked drifters (Niiler, personal communication, 1982), Doppler-acoustic values (Regier and Kosro, personal communication, 1982), and values from the XCP-measured average shear. The CTD values assume no motion at 1500 m (the velocities below 500 m are then <2 cm s^{-1}). The XBT values assume no motion at 500 m and a uniform T, S relation across the front; the CTD measurements show that this T, S assumption is consistent to within a 10% error in the velocity values, and imply that the position and width of the density front and jet coincide with those of the temperature front. The maximum Doppler-acoustic values measured appeared to be west of the surface temperature front; but, because the ship's track was almost parallel to the front for that section, it is difficult to compare the two signatures of the front. Only a single track was made, so it is not possible to separate geostrophic from inertial motions in these measurements. The XCP estimates are obtained by fitting a uniform vertical shear between 120 and 900 m in the individual profiles and assuming no motion at 900 m, then averaging over half-inertial period pairs to remove the influence of near-inertial waves. The values obtained by the different methods agree despite different depths-of-no-motion because the flow is weak below 300 m.

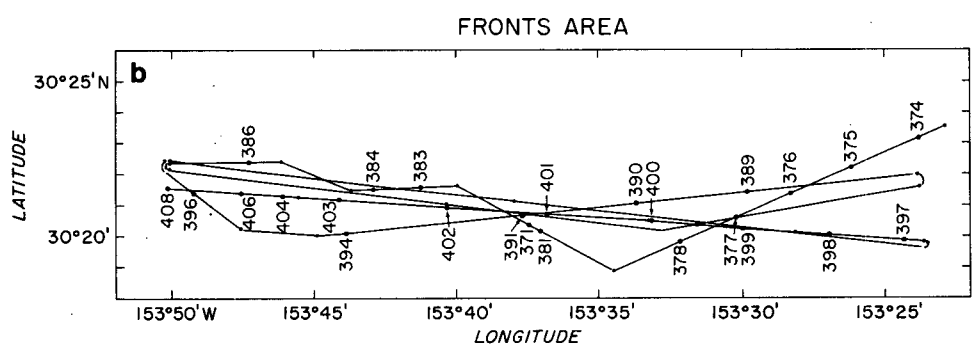

FIG. 2b. Three dense XCP sections taken across part of the front oriented north–south. The XCP drop positions are the numbered dots.

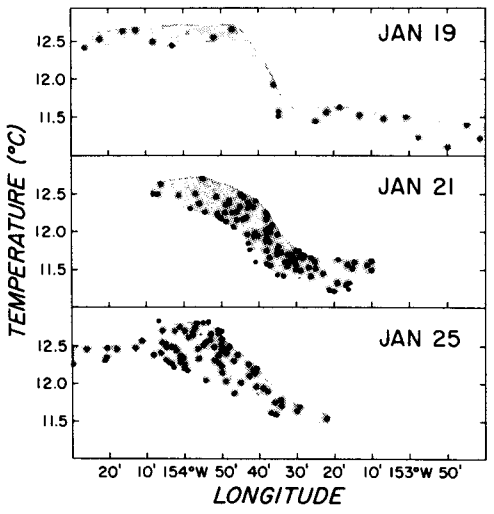

FIG. 3. XBT temperatures, averaged over 180–300 m, versus longitude across the front on 19, 21 and 25 January. The measurements made on 21 and 25 January are synoptic with the XCP measurements. The front is characterized by a temperature jump of 1°C over 20 km between 153°35′ and 50′W. Neither the position nor the intensity of the front changed significantly during the experiment.

The acrossfront circulation is at least an order of magnitude weaker than the alongfront flow. Ekman convergence is believed to be responsible for the enhanced gradients of midocean fronts such as the North Pacific Subtropical Front (Roden, 1975). Convergence was observed with satellite-tracked surface drifters (Niiler, 1982).

3. The velocity finestructure measurements

The velocity finestructure measurements were made with the expendable current profiler, XCP (Drever and Sanford, 1980). The XCP measures the two horizontal components of velocity and temperature to a depth of 900 m. Measurement of the motionally-induced voltage difference across two horizontally-separated electrodes allows velocity to be determined relative to an unknown but depth-independent constant (Sanford *et al.*, 1978). A measurement is made every 0.7 m. Averaging with a 7-m triangular window incremented at 3.5 m intervals provides velocity values every 3.5 m. The oceanic signal falls off as k_z^{-2} (where k_z is the vertical wavenumber) and drops below instrumental noise for wavelengths < 10 m (Dunlap *et al.*, 1981). For the Garrett and Munk spectrum, the horizontal internal wave velocities fall below XCP instrument noise for $\omega \gtrsim 10f$, so these measurements can only be used to examine the behavior of the low-frequency end of the internal wave band.

Temperature is measured with an XBT thermistor. Comparison with nearly simultaneous XBT profiles revealed average differences of 0.4°C, consistent with the XBT standard deviation error. Depth is taken to be a quadratic function of time since leaving the surface.

The upper 100 m of the profiles, corresponding to the mixed layer, were excluded from analysis because of contamination by surface swell and the electric field produced by the ship's cathodic protection. Bad points, defined as having an rms uncertainty > 5 cm s^{-1}, were also excluded.

The resulting profiles of relative velocity in the pycnocline are dominated by velocity finestructure with vertical scales > 80 m. This finestructure is interpreted as internal wave motions, and consequently the profiles were WKB-normalized with respect to the buoyancy frequency profile $N(z)$ (Fig. 4). WKB-scaling makes the profiles more homogeneous by removing variations in amplitude and vertical wavelength due solely to

TABLE 1. Estimates of the maximum surface velocity of the alongfront jet.

Instrument	Date (January)	Position	$V(z = 0)$ (cm s^{-1})
CTD	24–30	153°20–40′W	−22
XBT	19	153°35–50′W	−15
XBT	21	153°35–50′W	−22
XBT	25	153°35–52′W	−17
drifter	25	153°22′W	−12
drifter	28	153°45′W	−20
Doppler-acoustics	28	153°45–50′W	−25
XCP	21	153°30–40′W	−12
		estimated error	±5

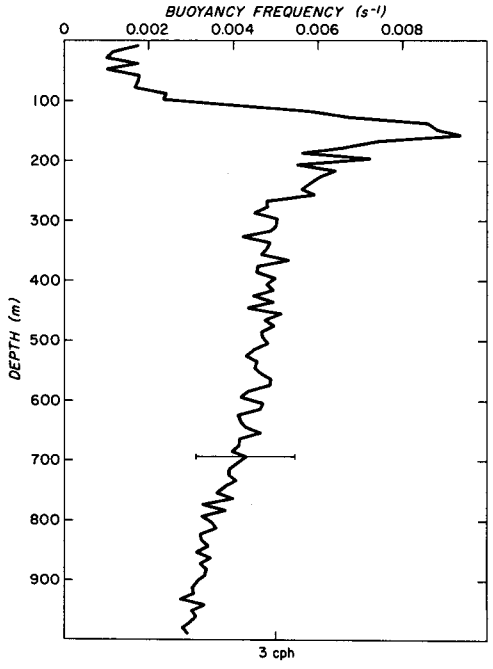

FIG. 4. The average buoyancy-frequency profile $N(z)$ in the front with the standard deviation at 700 m.

vertical changes in the buoyancy frequency. The WKB-normalization for internal waves is discussed by Leaman and Sanford (1975).

The buoyancy frequency profile did not vary significantly across the front. Unlike shelf fronts that separate tidally-mixed shelf water from stratified open ocean water and are characterized by strong horizontal gradients in the buoyancy frequency (Simpson *et al.*, 1978), the North Pacific Subtropical Front separates two open ocean regimes of similar stratification. The density contrast across the front is approximately 0.2‰ in the upper pycnocline (200 m) and becomes negligible by 500 m depth. The expected buoyancy frequency contrast is then only 10^{-3} s^{-1}, less than half the standard deviation of the buoyancy frequency at any depth; i.e., the buoyancy frequency contrast across the front is small compared to the random variability of the field.

The sampling strategy provided unaliased information about the spatial structure of the more energetic near-inertial waves. In all, 77 probes were dropped. The positions of the XCP drops are the numbered dots in Fig. 2a and the FRONTS area inset, detailed in Fig. 2b. The FRONTS area inset is a 50-km long section across the front mapped three times in half a day on 21 January (XCP 371–408). Profile separations of 2–4 km resolve the horizontal scales of the mean flow and near-inertial wave fields. The three sections were taken at ¼ an inertial period (6 h at 30°N) intervals to allow separation of near-inertial from noninertial motions. In addition to the east–west sections, a north–south transect was made to the northeast on 23 January (XCP 410–416) (Fig. 2a), several more profiles were taken in the inset area on 24 and 25 January (XCP 417–425), and two sections were made to the southwest of the front on 25–27 January (XCP 428–444). Three probes (XCP 445–447) were dropped 500 km to the south at 26°N, 156°W within a second front.

4. The internal wave field

This section discusses the velocity finestructure measured by the XCPs. Near-inertial motions with amplitudes of 10–20 cm s^{-1} dominate, consistent with the interpretation that the finestructure is internal wave motions. Most of the energy and its variability is in vertical wavelengths greater than 80 m. The average horizontal kinetic energy in the profiles is 4.0 J m^{-3}. Of this, roughly 2.7 J m^{-3} is propagating downward and 1.3 J m^{-3} upward. Two near-inertial features in the profiles contain most of the energy. The horizontal scales of both of these waves are ~O(10 km), similar to the width of the front.

Dominance of near-inertial motions is revealed in Fig. 5 which compares profiles taken 12 h apart. The energetic features are mirror-imaged, indicating dominance of near-inertial motions. In pair 381/401, most of the energy is in the *u*-component at a vertical wavelength of 500 m. In pairs 386/404 and 429/439, the more energetic waves have smaller vertical wavelengths of ~100 m. In all cases, the energetic features are near-inertial. To obtain a more quantitative measure of the fraction of near-inertial energy in the profiles, the half-inertial period pairs were summed and differenced to separate noninertial from near-inertial motions. Table 2 shows the energy in the resulting pair-sums (sub-inertial) and differences (inertial). Both components also contain noninertial internal wave energy. On average, the inertial component contains more than three quarters of the total kinetic energy in the profile.

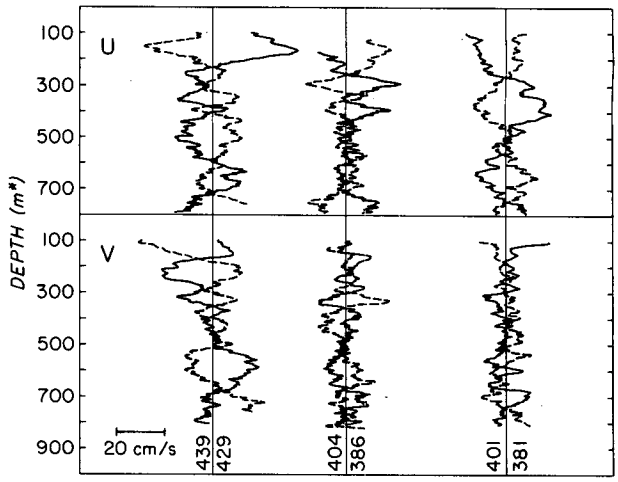

FIG. 5. Half-inertial period pairs 381/401 and 386/404 from 21 January and 429/439 from 26 January. The east velocity component u is plotted in the upper half, and the north component v in the lower half. Depth is in WKB-stretched meters. The more energetic features mirror-image each other at half an inertial period.

More energy is propagating downward than upward. The dominance of downward-propagating energy can be seen by comparing the energy in the rotary component turning clockwise-with-depth, i.e., the downward-propagating component, with that in the anticlockwise-with-depth, upward-propagating component. To obtain this result, a quadratic fit was removed from the WKB-normalized profiles to remove any low vertical wavenumber energy that would be poorly represented in the Fourier transform, before they were fast Fourier-transformed with a 12% split-sin^2 window. The complex FFTs yield real and imaginary components:

$$\left.\begin{aligned} u(z) &\rightarrow U_r(k_z) + iU_i(k_z) \\ v(z) &\rightarrow V_r(k_z) + iV_i(k_z) \end{aligned}\right\}. \qquad (1)$$

Restricting the tapering to a small fraction of the total profile preserves the energy of the profiles which were dominated by isolated energetic events. The Fourier transforms were decomposed into their clockwise-with-depth and anticlockwise-with-depth components (Gonella, 1972; Mooers, 1973):

TABLE 2. Energy in half-inertial period pair differenced and summed profiles.

Profile air	Inertial energy (J m^{-3})	Noninertial energy (J m^{-3})
371/391	1.5	0.6
374/397	1.2	0.8
376/398	2.2	0.6
381/401	1.2	0.8
383/402	1.9	0.7
386/404	3.1	0.7
386/406	2.5	1.3
429/438	5.3	1.2
429/439	6.2	0.4
429/440	5.9	0.8
average	3.0	0.8

$$\left.\begin{aligned} CW(k_z) &= [U_r(k_z) + V_i(k_z)] + i[U_i(k_z) - V_r(k_z)] \\ ACW(k_z) &= [U_r(k_z) - V_i(k_z)] + i[U_i(k_z) + V_r(k_z)] \end{aligned}\right\}. \quad (2)$$

Kinetic energy spectra were formed from these components and integrated over vertical wavenumber to determine the amount of energy propagating upward and downward. Fig. 6a shows the resulting rotary kinetic energies in J m^{-3} across the front. Downward-propagating energy dominates for all the profiles, as was observed by Leaman (1976) in the western North Atlantic.

More energy propagating downward than upward does not imply that the downward energy-flux is greater than the upward energy-flux. The energy-flux is a product of the energy and the group velocity, and the upward and downward group velocities may differ; i.e., if the upward and the downward-propagating energy are in different frequency–wavenumber waves. The upward and downward group velocities have been found to be different in the Sargasso Sea (D'Asaro and Perkins, 1984).

The most striking feature in Fig. 6a is the strong intensification of clockwise energy on the warm (western) edge of the front (Fig. 6b). This intensification is in the form of a sharp peak, rising by a factor of 4 above the background level of 1.6 J m^{-3} and having a half-energy width of 10 km. The peak appears in the same position on both 21 and 25 January. Comparison of the energetic profiles on the 2 days (for example, 386/404 and 429/439 in Fig. 5) reveals a similar vertical structure in the WKB-stretched depth range 250–400 m, but the later profiles are much more energetic at other depths. There also appears to be a slight deficit in clockwise energy in the cool (eastern) side of the front, but it is not statistically significant. Such intense spatial variability in internal wave kinetic energy (5 J m^{-3} over 5 km) has not previously been reported away from topographic features. Its proximity to a front suggests a dynamic link between the two phenomena.

The intensification is seen only in downward-propagating energy. Anticlockwise, upward-propagating energy is essentially uniform across the front. The enhancement of clockwise energy will later be shown to be due to an energetic downward-propagating near-inertial wave packet with a vertical wavelength of 100 m at 400 m depth.

The spatial variability in energy is contributed by wavelengths greater than 80 m. This can be seen by comparing energy-preserving spectra for profiles inside and outside the region of intensification (the peak) as in Fig. 7. Most of the energy lies under the clockwise, downward-propagating spectrum for profiles inside the peak (thick solid line). The anticlockwise, upward-propagating spectrum from the same profiles (long-dash line) lies well below it—but only for vertical wavelengths greater than 80 m. For smaller wavelengths there is equipartition of upward- and downward-propagating energy, and the spectra are identical to the Garrett and Munk clockwise/anticlockwise spectrum (Munk, 1981). The clockwise and anticlockwise spectra for profiles outside the region of intensification are the fine solid and short-dash lines respectively. The non-peak spectra and the anticlockwise spectrum in the region of intensification differ little from the Garrett and Munk clockwise/anticlockwise spectrum.

Equipartition of upward and downward-propagating energy at high vertical wavenumbers has been observed elsewhere in the ocean (D'Asaro, personal communication, 1983; Sanford, 1985), but D'Asaro and Perkins (1984) reported enhanced downward-propagating energy at all wavenumbers. McComas and Müller's

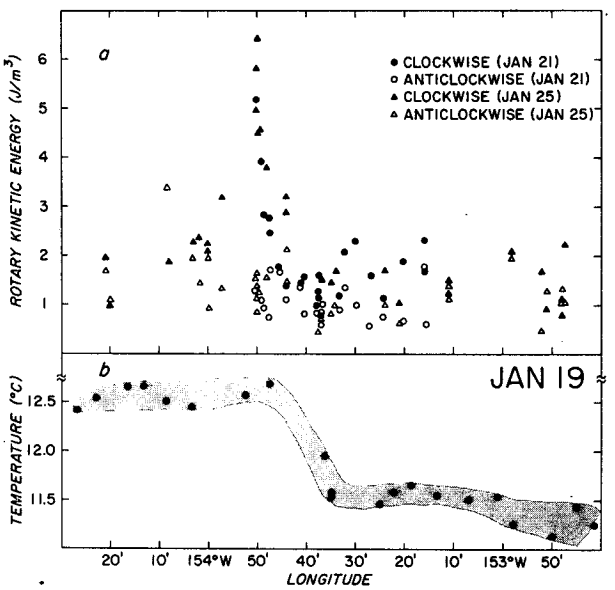

FIG. 6. Rotary kinetic energy across the front (a). Clockwise-with-depth (downward-propagating) energy dominates for all the profiles. Dramatic intensification of downward-propagating energy is seen on the warm (western) edge of the front (b). The peak did not change position or intensity between 21 and 25 January.

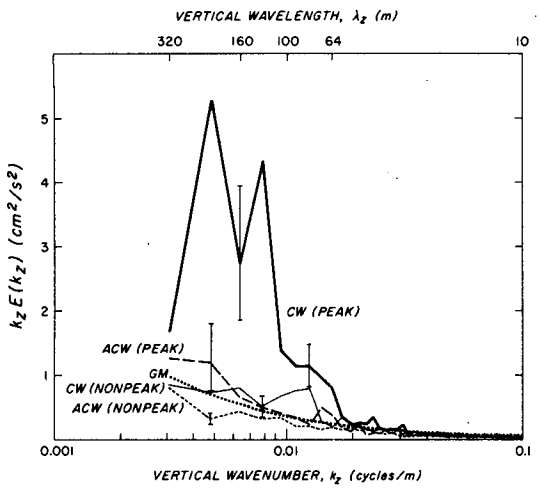

FIG. 7. Energy-preserving rotary spectra inside and outside the region of intensification (the peak). The clockwise-with-depth (downward-propagating) and anticlockwise-with-depth (upward-propagating) spectra for profiles in the region of enhanced downward-propagating energy (the peak) are the heavy solid and long-dash lines respectively. The clockwise and anticlockwise spectra outside the peak are the thin solid and short-dash lines respectively. The revised Garrett and Munk clockwise/anticlockwise spectrum (Munk, 1981) is the smooth line of dots.

(1981) computations indicate that vertical asymmetry at near-inertial frequencies will be enhanced rather than diminished by wave–wave interactions; the elastic scattering mechanism described by McComas and Bretherton (1977), where internal waves scatter off a wave of half their vertical wavelength to symmetrize upward and downward-propagating energies, is only effective at high frequencies.

The horizontal scales of the more energetic features can be estimated from correlations between horizontally-separated profiles. To reduce the effect of temporal evolution, the profiles were first rotated to a common time assuming an inertial rotation period. This is consistent with the dominance of near-inertial motions in the profiles evident in Fig. 5 and Table 2. A first order measure of the horizontal scale of the near-inertial motions is then the dropped rotated horizontal correlation coefficient,

$$\mathrm{cor}[u1, u2](\Delta x) = \langle u1u2\rangle/(\langle u1u1\rangle\langle u2u2\rangle)^{1/2}, \quad (3)$$

where Δx is the horizontal separation between measurements $u1$ and $u2$ and the averaging $\langle\ \rangle$ is over depth and over profile pairs having the same separation. The two rotated velocity components were treated separately. The correlation coefficient versus horizontal separation is shown in Fig. 8.

The rotated velocity components do not have the same horizontal structure. The v-component has a half-correlation length of 40 km. Its correlation coefficient falls off slowly, which suggests a narrowband process. In contrast, the u-component drops rapidly to a value of 0.8, characteristic of a broadband process, then decreases more slowly with a half-correlation length of 7 km. Note that the width of the front and the horizontal scales of the near-inertial waves are similar. The wave scales are an order of magnitude smaller than those measured in the mixed layer of the open ocean by Pollard (1980) and on the British Columbia continental shelf by Thomson and Huggett (1981). They are also smaller than typical values reported for the pycnocline (Kundu, 1976; Webster, 1968) and the conclusions of Fu (1981). This suggests that the front may be influencing the horizontal scale of the waves.

The dropped rotated horizontal coherence coh(k_z, Δx) provides a measure of the horizontal scale corresponding to different vertical wavelengths. For most energetic wavenumbers ($\lambda_z > 100$ m), the coherence behaved like the correlation coefficient. Vertical wavelengths less than 80 m had no significant coherence at even the smallest horizontal separations of 2 km.

There were two exceptions to this behavior (for $\lambda_z = 128$, 80 m). Fig. 9 displays the dropped, rotated horizontal coherence magnitude (|coh|), phase, and real part of coherence (coh$_r$) versus horizontal separation for the $\lambda_z = 128$ m clockwise-with-depth Fourier component. The stippling (upper frame) indicates the coherences not significantly different from zero. Phase is plotted only where the coherence magnitude is significant, i.e., up to separations of 90 km. The phase increases with separation (which is positive to the north and east), consistent with propagation to the south or west; the array acts as an antenna for waves propagating southwest (or northeast) but not in a perpendicular direction, so the direction of wave propagation could not be resolved any better. Consecutive zero-crossings of the phase suggest a horizontal wavelength of 30 km. This wavelength is also apparent in the undulations of the real part of the coherence (lower frame). By excluding different parts of the data set and recalculating the coherence, it was found that the undulating structure depended strongly on profiles from the west-

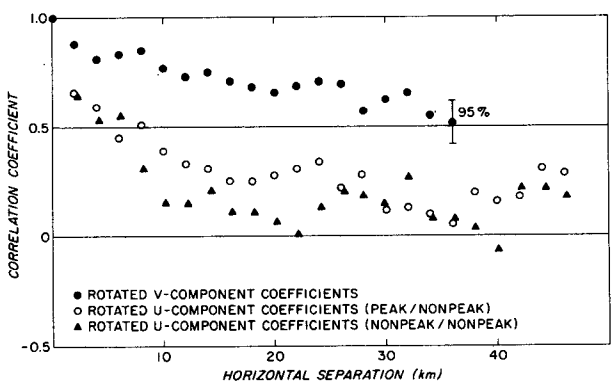

FIG. 8. Rotary correlation coefficient versus horizontal separation for the inertially-rotated horizontal velocity components. Averaging has been done over depth and over profile pairs having the same separation. The rotated v-component has a half-correlation length of ~40 km while the rotated u-component's is ~7 km.

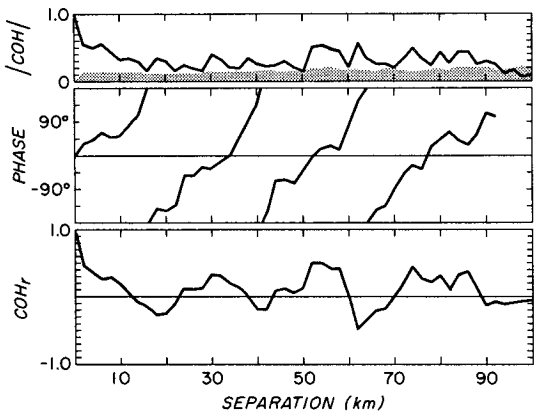

FIG. 9. Dropped rotated horizontal coherence magnitude |coh|, phase, and real part coh, versus horizontal separation for the λ_z = 128 m, clockwise-with-depth Fourier component. The stippling indicates the values not significantly different from zero at 95% confidence. The increasing phase with horizontal separation is consistent with a wavegroup propagating to the southwest. The horizontal wavelength of the packet is 30 km and the packet is at least $3\lambda_H$ long.

ern side of the three 21 January sections (Fig. 2b) and from the transect to the southwest (Fig. 2a; XCP 428–444) being included. This suggests that the wave is limited to the region west of the front's axis. The coherence for the λ_z = 80 m clockwise-with-depth component had similar structure.

In the following discussion, two dominant waves will be described: a low wavenumber standing wave in the rotated v-component responsible for the 40-km half-correlation length (Fig. 8), and an energetic, downward-propagating wavegroup responsible for the 10-km wide intensification of downward-propagating energy on the warm edge of the front seen in Fig. 6. The downward-propagating wave may be trapped and amplified through interactions with the front as will be put forward in the discussion. The low wavenumber wave is nonrotary with depth and may be reflecting off the surface.

a. The low-wavenumber wave

A low-wavenumber wave with a vertical wavelength of 500 m is responsible for the 40 km half-correlation length in the rotated v-component. Fig. 10 shows a section of inertially-rotated profiles, i.e., a synoptic snapshot of the spatial structure of the near-inertial wave field. Included are representative drops from each of the three 21 January XCP sections. The dominant feature in the rotated v-component of profile 383 is a sinusoid with a vertical wavelength of 500 m (corresponding to a mode 4 or 5 wave in a WKB-stretched ocean) with particle velocities of 10 cm s^{-1}. At this latitude, Henderschott (1973) predicts a mode 7 near-inertial wave with an amplitude of 7 cm s^{-1} due to scattering of the barotropic M_2 tide off bottom topography. But the absence of bottom relief and the limited spatial and temporal extent of this wave are not consistent with that source. This wave can be identified in adjacent profiles across most of the section and is probably responsible for the 40 km half-correlation length seen in the rotated v-component. Since the wave is near-inertial and therefore rotary in time (pair 381/401 in Fig. 5), its appearance in the v-component is due to the choice of the reference time.

Since its wavelength is on the order of the profile length, the wave's energy is not well represented by the spectra, which underestimate the cosine-amplitude because of the tapered windowing. Its contribution to the energy in Fig. 6 is also poorly represented. To get a better estimate of the wavelength and amplitude of the low wavenumber wave, the inertially-rotated velocity components were least-squares fit to sines and cosines in the pycnocline. Taking z = 0 at the base of the mixed layer, coefficients $U_r(\lambda_z)$, $U_i(\lambda_z)$, $V_r(\lambda_z)$, and $V_i(\lambda_z)$ were obtained for vertical wavelengths ranging from 300 to 600 m. The low-wavenumber wave in the rotated v-component appeared as a broad peak at λ_z = 500 m in the V_r coefficient (cosine). Fig. 11 shows the amplitude V (λ_z = 500 m) across the front in the upper frame. The stippling indicates the values not significantly different from zero at 95% confidence assuming V has a Gaussian distribution and 28 degrees of freedom. The amplitude is only significant between 153°23′ and 48′W, roughly the extent of the front. The phase (second panel) is only plotted where the amplitude is significant. It remains near zero across the front, consistent with dominance of the cosine fit; i.e., horizontal velocity crests at the base of the mixed layer.

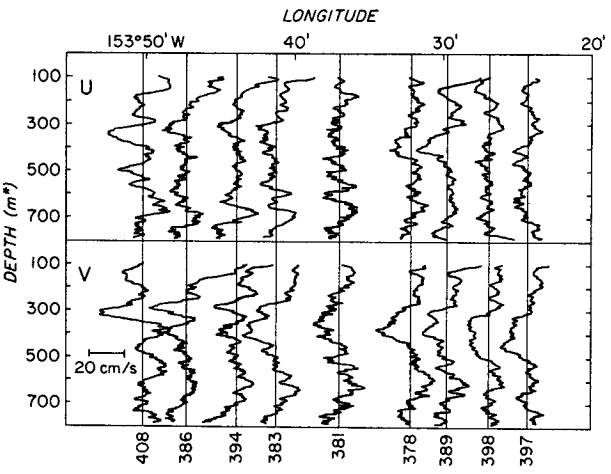

FIG. 10. A section of inertially-rotated, WKB-normalized velocity profiles across the front. The rotated u-component is plotted in the upper half, the rotated v-component in the lower half. Depth is in WKB-stretched meters. To the east, vertical wavelengths of 500 m are energetic in the rotated v-component with amplitudes of 7–10 cm s^{-1}; in the west, waves of 100 m vertical wavelength are energetic in both components with amplitudes of 20 cm s^{-1}.

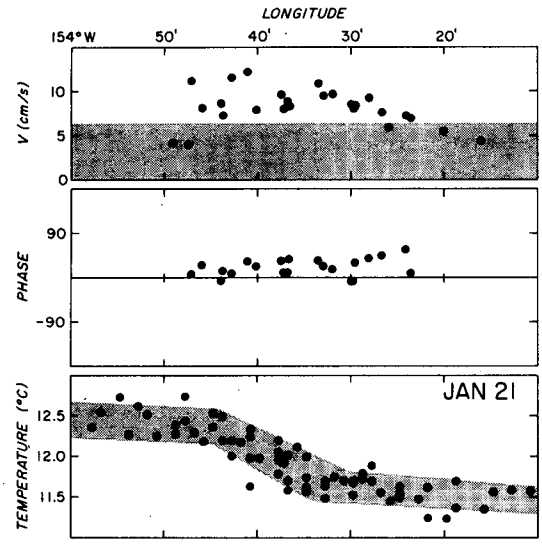

FIG. 11. Amplitudes and phases of the sine/cosine fits to the inertially-rotated v-component for a vertical wavelength of 500 m. The stippled band indicates the interval not significantly different from zero at 95% confidence. The fit is significant between 153°23' and 48'W. The phases are plotted only where the amplitude is significant.

This implies a node in vertical velocity at the base of the mixed layer (ruling out Ekman-pumping as a forcing mechanism but consistent with an upward-propagating wave reflecting off the surface), because vertical and horizontal velocities in a mode are vertically $\pi/2$ out-of-phase. A well-mixed layer will not support internal waves; wave velocities decay exponentially into the layer with a scale similar to the vertical wavelength in the pycnocline. For wavelengths much larger than the mixed-layer thickness, velocities in the mixed layer will be almost uniform, and the constraint of zero vertical velocity at the surface must also apply at the base of the mixed layer (D'Asaro, 1978).

Four and a half days later, on 25 January, none of the coefficients were significantly different from zero in the area; the low-wavenumber wave had moved on.

There is no turning of the velocity vector with longitude over the region where the wave has significant amplitude. This could not be the case if the wave were propagating in the east–west direction. Therefore, this wave must be propagating along the front. Unfortunately, there were no measurements spaced along the front, so the alongfront wavelength λ_y cannot be estimated.

The wave's velocity vector also does not turn with depth. This can be seen in Fig. 12, the hodograph of profile 390. The velocity vector describes a diagonal line in the u, v plane, consistent with the wave not propagating in the vertical. This would arise for an upward-propagating wave reflecting off the surface, since the superposition of an incident upward-propagating wave and the reflecting downward-propagating wave has the appearance of a standing wave in the upper pycnocline.

It is unlikely that this feature is a standing wave extending to the bottom. Because near-inertial waves propagate more rapidly in the horizontal than the vertical, the appearance of vertically-stationary waves can only occur during reflection of a wavegroup near the bottom (as has been reported by Fu, 1981; Lai, personal communication, 1983) or surface, or in the interior owing to the random superposition of upward- and downward-propagating wavegroups from unrelated sources. The latter possibility occurs rarely because near-inertial waves are very intermittent.

b. The downward-propagating wavegroup

Waves with vertical wavelengths of 100 m are responsible for the 7 km half-correlation length in the inertially-rotated u-component in Fig. 8. In the rotated u-component in Fig. 10, the more energetic features have vertical wavelengths of 100 m and are coherent over only a few adjacent profiles.

A downward-propagating wavegroup is responsible for the intensification of clockwise energy on the warm (western) edge of the front in Fig. 6a. The feature is seen at 300–400 m depth in the west in Fig. 10 (XCP 386, 394, 408). It has a strong signature (amplitudes of 20 cm s^{-1}) in both u- and v-components. The hodograph of profile 408 (Fig. 13) shows the velocity

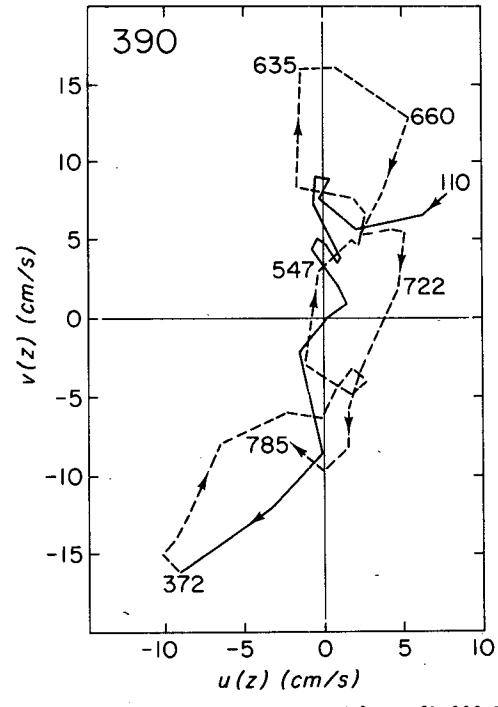

FIG. 12. The hodograph of $v(z)$ versus $u(z)$ for profile 390. Labeled depths are in WKB-stretched meters. The velocity vector describes a diagonal line (degenerate ellipse) consistent with a vertically-stationary wave having a vertical wavelength of 500 m.

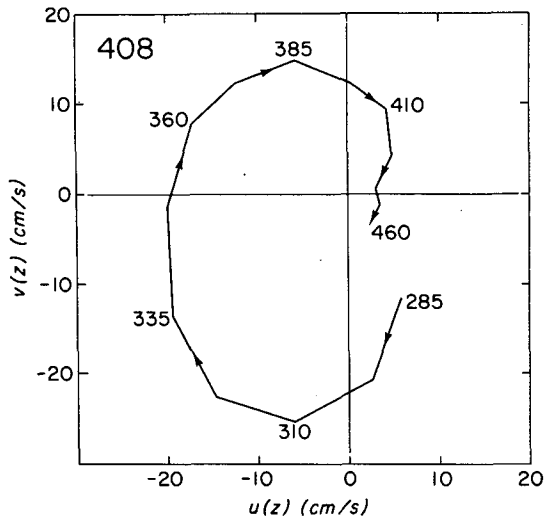

FIG. 13. The hodograph of profile 408 on the warm edge of the front. Depths are given in WKB-stretched meters. The velocity vector turns clockwise-with-depth, as would be the case for a downward-propagating wave.

vector turning clockwise with depth from 285–460 m, consistent with downward-propagation.

In addition to being downward-propagating, the wavegroup appears to be propagating to the west. Internal waves propagate along lines of constant phase, and the wavegroup's constant phase lines slope downward to the west. This can be seen in Fig. 14a which includes all the profiles taken in the energetic wave inertially-rotated to a common time. The wavecrests (solid circles) deepen to the west, appearing to deepen more rapidly west of profile 404. The ensemble-averaged depth for each of the extrema is indicated along the right axis.

The deepening of the crests can be fit to two significantly different slopes to the east and west of profile 404. The procedure is shown schematically in Fig. 14b. The ensemble-averaged depths were removed for each of the extrema and the resulting relative depths combined. Then these relative depths were equally weighted in a least-squares fit to a straight line. Profiles east and west of profile 404 were fit separately. In Fig. 14b the solid lines are the least-squares estimate of the slope, and the dashed lines bracket the 90% confidence interval around the slope. West of profile 404 the slope $S_x = 5.7 \pm 1.5$ ($\times 10^{-3}$) m m^{-1} ($=k_x/k_z$); east of 404 $S_x = 1.3 \pm 2.3$ ($\times 10^{-3}$), not significantly different from zero. These values can be compared with the 400-m depth isothermal (isopycnal) slopes of $(d\rho/dz)/(d\rho/dx) \leq 10^{-3}$ from the XBT sections. The change in phase slope is not consistent with a wave propagating in a homogeneous medium and suggests the wave is becoming less inertial away from the center of the front. It should be pointed out that the wave is still near-inertial (within 10%) so that using inertially-rotated pairs collected over half an inertial period does not introduce serious systematic errors.

The vertical wavelength of the wave was estimated to be $\lambda_z = 120 \pm 30$ m by averaging the separations between consecutive maxima and minima in each profile.

Other measurements during FRONTS '80 also found anomalously energetic near-inertial waves in fronts. The three profiles taken 500 km to the south of the experimental site (XCP 445–447) were on the warm side of a second front at 26°N and are as energetic as the profiles in the peak.

c. *Other features of the internal wave field*

There is no indication of any directionality in the high-frequency waves in the front. Coherences as a function of vertical wavenumber were calculated between the vertical temperature gradient and velocity shear. As in Johnson and Sanford (1980), the horizontal temperature gradient is sufficiently small that interaction between it and horizontal internal wave motions

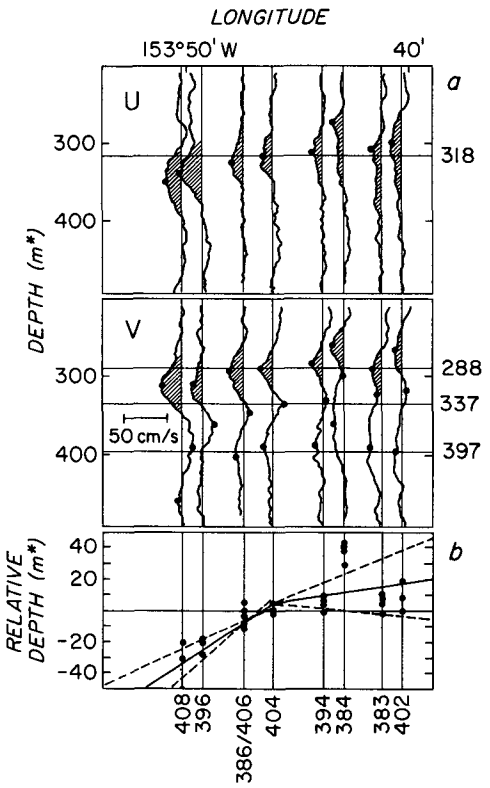

FIG. 14. (a) A section of all the profiles, inertially-rotated and WKB-normalized, taken within the energetic wavegroup. The wavecrests (solid circles) deepen to the west. The ensemble-averaged depth for each crest is given along the right axis. (b) The least-squares fit (solid line) and the 90% confidence limits (dashed lines) of the phase slope. The slopes were calculated separately for the profiles east and west of profile 404. West of 404 the slope is downward to the west. East of 404, the slope is not significantly different from zero.

is negligible compared with the interaction between the vertical temperature gradient and vertical internal wave motions. Since the front is noncompensating, there can be no double-diffusive intrusions (Garrett and Horne, 1978). Significant coherences can then be attributed to directional waves, and the direction deduced from the phase behavior. For propagating high-frequency waves, coherence will be found with the velocity component along the propagation axis with phase $\pm \pi/2$ depending on the direction of propagation. For propagating near-inertial waves, coherence will occur with both components; the phase will be $\pm\pi/2$ for the velocity component in the direction of propagation and 0 or π for the perpendicular component. No consistent phase behavior was found where the coherence was significant. This agrees with the results of Johnson and Sanford who found no directionality associated with open-ocean mean flow shear.

A brief statement about the statistics of these measurements should be made. For a horizontal length scale of ~20 km (suggested by the half-correlation length of 7 km), a vertical length scale of 200 m, and a propagation time scale of 10 days [suggested by other measurements (Pollard and Millard, 1970) and consistent with the features seen during FRONTS '80], the 100-km and 4-day span of the experiment contains no more than 12 independent realizations of the near-inertial field. Two of these include the energetic profiles on the warm edge of the front seen on 21 and 25 January—another, the low-wavenumber sinusoid within the front seen on 21 January but not in later measurements. Another realization is added by the energetic feature observed in the second front 500 km to the south. From such a limited sample, one cannot draw any conclusions about the typicalness of such features in fronts.

5. Discussion

The discussion will focus on the characteristics of the energetic downward-propagating wavegroup (Fig. 6) observed on the warm edge of the front and on explaining its presence in the front. The estimates of the vertical wavelength λ_z and the slope of constant phase lines S_x (Fig. 14) can be used to estimate the wave's acrossfront wavelength, frequency, and group velocity by assuming the alongfront wavenumber $k_y = 0$. This assumption will result in an underestimate of the wave's frequency and vertical group velocity. Considering only the steeper part of the slope west of profile 404 (Fig. 14b), and neglecting, for the moment, interaction with the mean flow shear, the acrossfront wavelength is given by

$$\lambda_x = \frac{\lambda_z}{S_x} = 20 \pm 13 \text{ km}. \tag{4}$$

The frequency for internal waves is

$$\omega = f(1 + \epsilon) = \frac{[N^2(S_x^2 + S_y^2) + f^2]^{1/2}}{(S_x^2 + S_y^2 + 1)^{1/2}}, \tag{5}$$

which for near-inertial waves simplifies to

$$\epsilon \approx \frac{N^2}{2f^2}(S_x^2 + S_y^2) \geqslant \frac{N^2 S_x^2}{2f^2} = 0.08 \pm 0.04, \tag{6}$$

i.e., within 10% of the Coriolis frequency f. This is the intrinsic frequency of the wave irrespective of the mean flow, not the Doppler-shifted frequency that would be measured by a current meter mooring. The vertical group velocity is

$$|Cg_z| \approx \frac{N^2\lambda_z}{2\pi f}(S_x^2 + S_y^2) \geqslant \frac{N^2\lambda_z S_x^2}{2\pi f} = 19 \pm 17 \text{ m day}^{-1}. \tag{7}$$

This value implies that the wave would have taken ~3 weeks (overestimate) to propagate from the base of the mixed layer to a depth of 400 m. The horizontal group velocity in the x-direction is

$$|Cg_x| \approx \frac{N^2\lambda_z S_x}{2\pi f} = 3.4 \pm 1.9 \text{ km day}^{-1}, \tag{8}$$

implying that the wave would have taken 1–2 weeks to cross the 30-km wide front in the absence of wave–mean flow interactions.

The wavegroup is not linear. For a near-inertial wave to be linear, $\partial u/\partial t = fu \gg u\partial u/\partial x$ or

$$\frac{f\lambda_x}{2\pi u} \gg 1.$$

Here, $f = 7 \times 10^{-5}$ rad s^{-1}, $u = 20$ cm s^{-1}, and $\lambda_x = 20$ km, yielding $f\lambda_x/(2\pi u) \simeq 1$. This parameter is also a measure of the ratio of the orbital radius to the horizontal wavelength, and of the particle velocities to the phase velocity of the wave.

In addition, the wavegroup's vertical shear is only marginally stable because the wave's Richardson number

$$\text{Ri} = \frac{N^2}{k_z^2 u^2} \approx 0.25 \tag{9}$$

for a vertical wavelength $\lambda_z = 120$ m, an amplitude of 20 cm/s and a buoyancy frequency $N = 0.005$ s^{-1}.

The remainder of the discussion will focus on examining possible origins of the energetic wavegroup. There are a number of explanations:

i) generation during geostrophic adjustment
ii) wind generation
iii) enhancement by wave-mean flow interactions.

While all three of these mechanisms are plausible, the last mechanism produces the results that are most consistent with the observations.

Near-inertial waves might be generated during geostrophic adjustment following barotropic (drawing energy from the geostrophic kinetic energy) or baroclinic (drawing from the mean potential energy) instability as has been observed in laboratory experiments (Griffiths, personal communication, 1983). The geostrophically energetic upper pycnocline and mixed layer contained features with scales ~O(1 km) (Paulson *et al.*, 1980), small enough to be unstable for the observed velocities. One of the XBT sections revealed a transient warm–cold core pair on the warm edge of the front reminiscent of the vortex-pair structures formed during instability of laboratory flows (Griffiths and Linden, 1981).

The wavegroup is energetic enough to be important to the dynamics of the front. It has kinetic energy density ~ 20 J m^{-3}, comparable to the energy stored in the front. If the front were to double in intensity [as it was observed to do in the week following the XCP measurements (Roden, 1981)], there would be changes in potential and kinetic energy of 0.06 and 60 J m^{-3} in the mixed layer and 240 and 3 J m^{-3} in the upper 100 m of the pycnocline. Thus, there is sufficient energy to have generated the wave in the front's kinetic energy in the mixed layer and in the front's potential energy in the upper pycnocline. Below 200 m depth, neither the geostrophic density nor flow fields contain sufficient energy to account for the wave.

The wavegroup's energy-flux is given by

$$F_{iw} \approx CgE \geqslant Cg_xE \geqslant \frac{N^2KE\lambda_z S_x}{2\pi f}$$

$$= 0.8 \pm 0.6 \text{ W m}^{-2} \text{ (underestimate)}, \quad (10)$$

and is mostly in the horizontal. The corresponding vertical flux is 40 ± 30 ($\times 10^{-4}$) W m^{-2}, an order of magnitude larger than Leaman's (1976) estimate of 2.4×10^{-4} W m^{-2} and Käse and Olbers' (1979) estimate of 4×10^{-4} W m^{-2}. If this vertical energy-flux was allowed to accumulate in a 100-m thick layer, it would take roughly two months for the near-inertial energy to match the available potential energy in the upper 100 m of the pycnocline and substantially less time in the deeper pycnocline. Therefore, any exchange of energy between the mean flow and this wavegroup could contribute to deepening or shallowing the front.

Wind-forcing cannot be ruled out as the generation mechanism responsible for the wave. If we equate the wave's vertical energy-flux with the maximum influx of energy from the wind,

$$F_w = V_0 \rho_{\text{air}} C_D V_w^2, \quad (11)$$

where V_w is the wind speed, $V_0 = 20$ cm s^{-1} is the amplitude of the wave, and $C_D = 1.3 \times 10^{-3}$, wind speeds of $\geqslant 4 \pm 2$ m s^{-1} are needed to produce the observed energy-flux. An additional constraint to ensure the energy goes into the inertial wave field is that the wind vector turn clockwise in time over periods of less than a day. Wind events with appropriate time scales had magnitudes > 15 m s^{-1} at least once a week in the 2 months preceding the experiment. Therefore, there is more than sufficient energy in the wind field to account for the energetic wave. A further property of wind generation is that the horizontal scale of the waves should be similar to the wind scale. Therefore, to explain the short horizontal scales of the energetic wavegroup in terms of wind generation requires either

i) an intense wind event on scales $\sim$ O(10 km) [such features are associated with cold front storms (Hobbs *et al.*, 1980)] or

ii) mechanisms acting to reduce the wave scales in the ocean.

Interaction with the alongfront jet could alter the scales of near-inertial waves and could account for the enhanced downward-propagating near-inertial wave energy on the warm side of the front. Kunze (unpublished manuscript) formulated a dispersion relation for near-inertial waves propagating in geostrophic shear, generalizing the relation found by Mooers (1975). The wave's intrinsic frequency is given by

$$\omega_0 = \omega - (\mathbf{k} \cdot \mathbf{V}) = f_{\text{eff}} + \frac{N_{\text{eff}}^2 k_H^2}{2f k_z^2}, \quad (12)$$

where the effective Coriolis frequency

$$f_{\text{eff}} \approx f + \frac{1}{2}\left(\frac{\partial V}{\partial x} - \frac{\partial U}{\partial y}\right), \quad (13)$$

is the planetary value of the Coriolis frequency perturbed by half the geostrophic vorticity, $\zeta = (\partial V/\partial x - \partial U/\partial y)$; physically, the wave feels the fluid's as well as Earth's rotation. The effective buoyancy frequency,

$$N_{\text{eff}}^2 = N^2 + 2g\frac{\partial \rho}{\partial x}\frac{k_x k_z}{k_H^2} + 2g\frac{\partial \rho}{\partial y}\frac{k_y k_z}{k_H^2}, \quad (14)$$

depends on both vertical and horizontal density gradients, and the direction of propagation (wavevector direction). It represents the total density contrast encountered by a fluid parcel as it traverses its orbit. Dispersion relation (12) is similar to the internal wave dispersion relation for near-inertial waves in the absence of mean flow, but the Coriolis and buoyancy frequencies have been altered by the geostrophic shear.

To determine the influence of geostrophic shear on near-inertial wave propagation, waves were propagated into a model baroclinic jet analogous to the North Pacific Subtropical Front (upper frame in Fig. 15) using a ray-tracing approach. The details of the method are given in Kunze (unpublished manuscript). The effective Coriolis frequency associated with the jet is shown

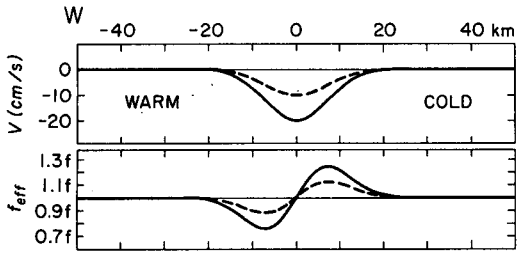

FIG. 15. A model southward baroclinic jet analogous to the North Pacific Subtropical Front (upper frame), and the associated effective Coriolis frequency $f_{eff} = f + \zeta/2$ (lower frame). The solid curves are values at the surface and the dashed curves at a depth of 100 m. Internal waves propagate freely only for frequencies lying above the f_{eff} curve.

in the lower frame of Fig. 15. It is antisymmetric across the front with a negative vorticity trough on the warm (western) side and a positive vorticity ridge on the cool (eastern) side of the jet.

The effective Coriolis frequency is the lower bound of the internal waveband; i.e., internal waves propagate freely only for frequencies lying above the curve describing f_{eff}. This suggests that near-inertial waves (where near-inertial is taken to be near the effective Coriolis frequency) in the negative vorticity trough will have frequencies below the effective Coriolis frequency outside this region, so will be unable to propagate out.

In Fig. 16, the ray paths are shown for waves propagating downward from the surface consistent with wind generation (Pollard and Millard, 1970; Krauss, 1976) into the model flow. All waves start at the surface with an initial vertical wavelength of 100 m and an acrossfront wavelength of 40 km corresponding to $\epsilon = (\omega_0 - f_{eff})/f_{eff} = 0.06$. The influence of the Doppler-shift ($\mathbf{k} \cdot \mathbf{V}$) is eliminated by setting the alongfront wavenumber equal to zero (normal incidence). Waves originating in the negative vorticity trough on the western side of the jet cannot escape (Fig. 15). They become more inertial as they try to propagate out of the trough due to the higher effective Coriolis frequency on either side. To continue to satisfy the dispersion relation (12), the wavevector must change. In general, only the component of the wavevector in the direction of the gradient (in the internal waves' environment) is affected. As the wave tries to propagate out of the side of the trough, the acrossfront wavenumber decreases (consistent with the wave becoming more inertial), passing through zero at the turning point, and the wave is reflected. The wave encounters turning points at either side of the negative vorticity trough.

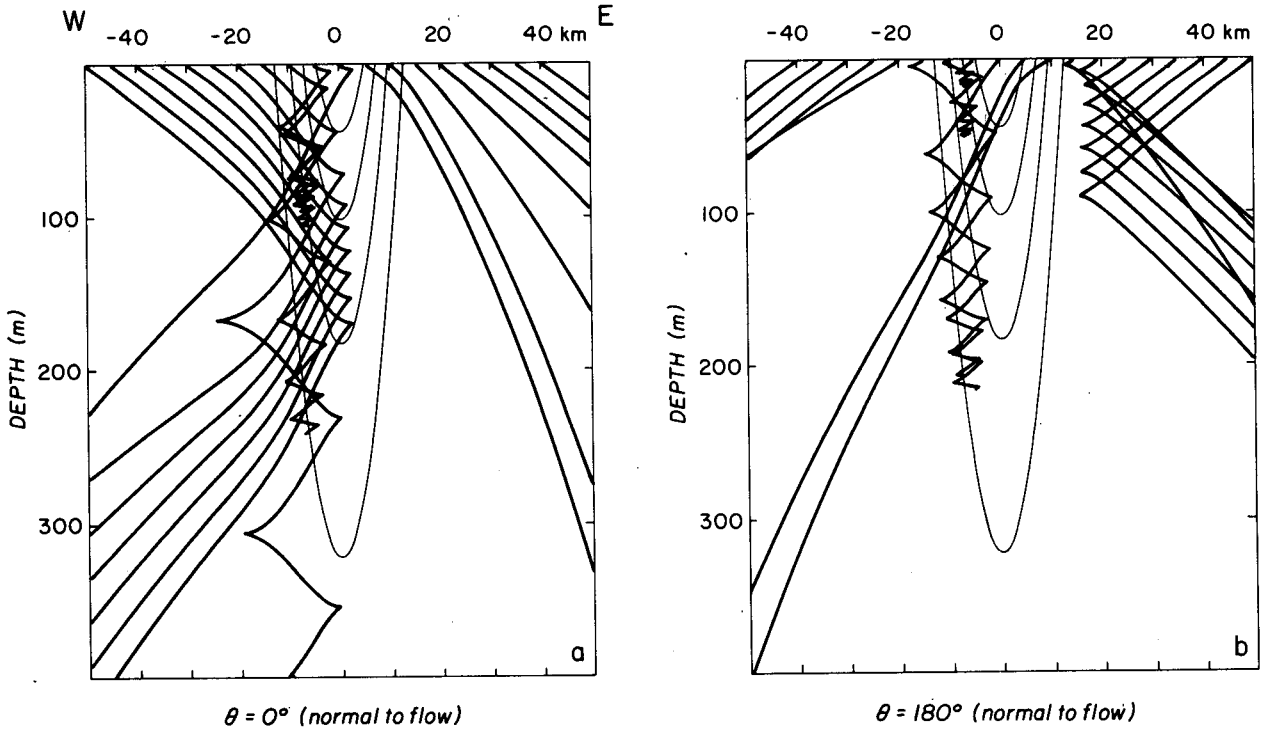

FIG. 16. Ray paths (thick solid lines) for near-inertial waves propagating into a baroclinic jet. The thin lines are isotachs. Flow is out of the page. The horizontal wavevector is given by $(k_x, k_y) = k_H(\cos\theta, \sin\theta)$ where k_x is the acrossfront and k_y the alongfront wavenumber. The two cases shown above are for normal incidence on the front ($k_y = 0$). Waves originating outside the jet are deflected away from the positive vorticity ridge on the eastern side of the front (Fig. 15). Waves originating in the negative vorticity trough on the western side of the jet have intrinsic frequencies below the effective Coriolis frequency of the neighboring ocean so are trapped in the trough. These waves stall at their critical depth where the effective Coriolis frequency is equal to their intrinsic frequency.

As it propagates downward, it also encounters an increasingly effective Coriolis frequency in the vertical, since the geostrophic vorticity weakens with depth. This also acts to make the wave more inertial, and the vertical wavelength shrinks to satisfy the dispersion relation (12). At the critical depth, where the effective Coriolis frequency equals the wave's intrinsic frequency, the vertical wavelength and group velocity go to zero and the wave stalls. Consistent with conservation of action flux, amplification of the wave occurs as the vertical group velocity diminishes. Both the amplification and the shrinking vertical wavelength enhance the wave shear and the likelihood of internal wave breaking. The marginal stability of the observed wave is consistent with this result as are the turbulent shear measurements of Lueck (1982) in a warm-core ring. He found dissipation levels 1000 times higher than usually observed in the pycnocline at the base of the negative vorticity core. Dissipation profiles collected during the FRONTS '80 experiment (Lueck and Osborn, 1982) did not reveal enhanced dissipation in the vicinity of the front; however, it is not clear that any of their measurements were made in regions of negative vorticity.

This interaction mechanism traps only waves originating *inside* regions of negative vorticity. Thus, the low-mode wave, which propagated into the front from below, will not be trapped. It is tempting to identify the intense wavegroup on the warm edge of the front (Fig. 14) with the undulations of similar scales in the horizontal coherence (Fig. 9). This would not be consistent with amplification and trapping by wave–mean flow interactions. The coherent structure occurred only in profiles west of the front axis, suggesting that this feature may correspond to the waves originating outside the jet in Fig. 16a that pass through the negative vorticity trough but are deflected by the positive vorticity ridge. The westward propagation of the observed feature suggests it has already been reflected. Alternatively, the trapped wave may be losing energy by wave–wave interactions to a slightly higher frequency wave which is free to radiate away.

Trapping and critical-layer amplification occur only on the negative vorticity side of the jet in Fig. 16. In the positive vorticity ridge on the eastern side of the jet, near-inertial waves have frequencies above f_{eff} everywhere, so are free to propagate out; however, near-inertial waves trying to penetrate the ridge from outside are deflected by turning points.

The influence of the effective buoyancy frequency is weak for the model flow used here. Its effect is to tilt particle motion into the plane of the isopycnals, as can be seen in the upturning of the turning point cusps in Fig. 16 near the center of the jet where the isopycnal slopes are steepest.

6. Conclusions

Downward-propagating, near-inertial waves with vertical wavelengths greater than 80 m and horizontal scales of ~O(10 km) dominated profiles of the velocity finestructure collected in the North Pacific Subtropical Front in January 1980. Lack of coherence between the vertical temperature-gradient and velocity shear suggests that there is no preferred directionality to the high-frequency internal waves; i.e., the noninertial internal wave field is horizontally isotropic in the front.

There was considerable spatial variability in the near-inertial wave energy, though there were too few realizations to make a statistical comparison of the internal wave field inside the front with that away from the front. On the warm (western) edge of the front, an intense peak in downward-propagating energy was observed (Fig. 6). The peak was ~10 km wide and rose by a factor of 4 above the background internal wave energy level. The feature responsible for this enhancement was a wavegroup with a vertical wavelength of 120 m and an acrossfront wavelength of 20 km. It was observed at 400 m depth propagating downward and away from the front (Fig. 14). This wave was nonlinear and its vertical shear only marginally stable. Its energy was comparable to that stored in the front. The change in its phase slope (Fig. 14) was not consistent with wave propagation in a homogeneous medium, suggesting interaction with the front.

Away from this feature but still in the front, the profiles were dominated by a low-wavenumber (λ_z = 500 m) near-inertial wave (Fig. 11) that may be in the process of reflecting off the surface (i.e., vertically stationary in the upper 900 m with a node in vertical velocity at the surface extending through the mixed layer). It was argued that this wave was propagating along the front.

Possible causes of the energetic wavegroup on the warm side of the front were explored. The wavegroup was energetic enough to influence the dynamics of the front. Whether it was the result of wind generation or interaction with the front could not be determined, but the discovery of a similarly energetic wave in another front suggests these features may be common in fronts.

Modeling near-inertial wave interaction with the vorticity field associated with the alongfront jet reproduces the following features:

i) amplification of downward-propagating, near-inertial energy on the warm side of the front,

ii) a flux of energy from lower to higher vertical wavenumbers that should push the low wavenumber spectral peak at $\lambda_z \sim 500$ m to higher wavenumbers,

iii) marginally stable vertical shear, and

iv) a deficit of downward-propagating, near-inertial energy on the cool side of the front.

All of these model results are consistent with the FRONTS '80 observations.

In an analytical study, Paldor (1983) has found a trapped inertial mode for the special case of a constant potential vorticity surface layer front over a passive, infinitely deep lower layer.

The fate of the trapped near-inertial energy was not resolved. WKB wave–mean flow interaction would allow near-inertial energy to pile up indefinitely and this is clearly unrealistic; there must be a sink. Two possible sinks are:

i) internal wave-breaking and turbulent dissipation, and

ii) loss to higher-frequency internal waves by wave–wave interactions.

Which of these sinks dominates may profoundly affect the relaxation of geostrophic flows and the internal wave field. Wave-breaking could play a major role in dissipation of both internal wave and geostrophic energy. Energy lost to higher-frequency internal waves would be free to disperse away from the trapping region.

This research has shown that intense intermittency in the near-inertial wave field exists on horizontal scales $\sim$ O(10 km) and vertical scales $\sim$ O(100 m) and suggests that this inhomogeneity is due to interaction with the vorticity field of geostrophic flow. Wave–mean flow interactions transform both the vertical and horizontal scales of waves; this may in part explain the presence of relatively small scales [$\sim$O(10 km)] in the pycnocline while the mixed layer is dominated by much larger scales [$\sim$O(100 km)]. Whether energetic near-inertial waves are a common feature of fronts or to what extent this trapping mechanism is responsible for the observed intermittency of near-inertial waves was not resolved. However, previous profiles from over the Caryn Seamount and recent measurements in a warm-core ring also reveal intense, downward-propagating, near-inertial motions at the base of regions of geostrophic negative vorticity, and energetic near-inertial packets have been observed on the warm sides of passing fronts in the LOTUS array (Briscoe, personal communication, 1983).

Acknowledgments. The research was conducted with the assistance of personnel of NOAA's OSS *Oceanographer.* We wish to acknowledge their help and that of the Chief Scientist, S. Hayes. A. Bartlett and J. Dunlap are commended for their help in the deployment of the probes under adverse conditions. We are indebted to G. Roden, S. Hayes and P. Niiler for making unpublished data available, and to W. Emery for digitizing the XBT data. Valuable insight and advice were gained from discussions with E. D'Asaro, B. Elliott, N. Larson, T. Shay and J. Dunlap. This research was funded under ONR Contract N00014-80-C-0252.

REFERENCES

Brown, E. D., and W. B. Owens, 1982: Observations of the horizontal interactions between the internal wave field and the mesoscale flow. *J. Phys. Oceanogr.*, **11,** 1474–1481.

Csanady, G. T., 1978: Wind effects on surface to bottom fronts. *J. Geophys. Res.*, **83,** 4633–4640.

D'Asaro, E. A., 1978: Mixed layer velocities induced by internal waves. *J. Geophys. Res.*, **83,** 2437–2438.

——, and H. Perkins, 1984: A near-inertial wave spectrum for the Sargasso Sea in late summer. *J. Phys. Oceanogr.*, **14,** 489–505.

Drever, R. G., and T. B. Sanford, 1980: An expendable temperature and velocity profiler (XTVP). *Proc. Near-Surface Ocean Experimental Technology Workshop,* NORDA 163–173.

Dunlap, J. H., R. G. Drever and T. B. Sanford, 1981: Experience with an expendable temperature and velocity profiler (XTVP). *Conf. Record Oceans '81,* Boston, 372–376.

EOS Transactions, 1980: *Upper Ocean Fronts Abstracts. AGU,* **61(46),** 1000–1002.

Frankignoul, C., 1976: Observed interaction between oceanic internal waves and mesoscale eddies. *Deep-Sea Res.*, **23,** 805–820.

——, and T. M. Joyce, 1979: On internal wave variability during the Internal Wave Experiment (IWEX). *J. Geophys. Res.*, **84,** 769–776.

Fu, L.-L., 1981: Observations and models of inertial waves in the deep ocean. *Rev. Geophys. Space Phys.*, **19,** 141–170.

Garrett, C., and W. Munk, 1972: Space-time scales of internal waves. *Geophys. Fluid Dyn.*, **2,** 225–264.

——, and ——, 1975: Space-time scales of internal waves: A progress report. *J. Geophys. Res.*, **80,** 291–297.

——, and E. Horne, 1978: Frontal circulation due to cabbeling and double diffusion. *J. Geophys. Res.*, **83,** 4651–4656.

Gonella, J., 1972: A rotary-component method for analyzing meteorological and oceanographic vector time-series. *Deep-Sea Res.*, **19,** 833–846.

Griffiths, R. W., and P. F. Linden, 1981: The stability of vortices in a rotating, stratified fluid. *J. Fluid Mech.*, **105,** 283–316.

Hayes, S. P., 1979: Benthic current observations at Domes sites A, B and C in the tropical North Pacific. *Marine Geology and Oceanography of the Pacific Manganese Nodule Province,* J. L. Bischoff and D. Z. Piper, Eds., Plenum Press, 83–112.

Henderschott, M. C., 1973: Inertial oscillations of tidal period. *Progress in Oceanography,* Vol. 6, Pergamon, 1–27.

Hobbs, P. V., T. J. Matejka, P. H. Herzegh, J. D. Locatelli and R. A. Houze, Jr., 1980: The mesoscale and microscale structure and organization of clouds and precipitation in midlatitude cyclones. I: A case study of a cold front. *J. Atmos. Sci.*, **37,** 568–596.

Johnson, C. L., and T. B. Sanford, 1980: Anomalous behavior of internal gravity waves near Bermuda. *J. Phys. Oceanogr.*, **10,** 2021–2034.

Käse, R. H., and D. J. Olbers, 1979: Wind-driven inertial waves observed during Phase III of GATE. *Deep-Sea Res.*, **26(Suppl.),** 191–216.

Krauss, W., 1976: On currents, internal and inertial waves in a stratified ocean due to variable winds, Part 1. *Dtsch. Hydrogr. Z.*, **29,** 87–135.

Kundu, P. K., 1976: An analysis of inertial oscillations observed near Oregon coast. *J. Phys. Oceanogr.*, **6,** 879–893.

Kunze, E., 1985: Near-inertial wave propagation in geostrophic shear. (Unpublished manuscript).

Leaman, K. D., 1976: Observations of the vertical polarization and energy flux of near-inertial waves. *J. Phys. Oceanogr.*, **6,** 894–908.

——, and T. B. Sanford, 1975: Vertical energy propagation of inertial waves: a vector spectral analysis of velocity profiles. *J. Geophys. Res.*, **80,** 1975–1978.

Leetmaa, A., and A. D. Voorhis, 1978: Scales of motion in the subtropical convergence zone. *J. Geophys. Res.*, **83,** 4589–4592.

Lueck, R. G., 1982: Dissipation in a warm core ring. *EOS Transactions,* **63(42),** 999.

——, and T. R. Osborn, 1982: Dissipation measurements from the FRONTS '80 expedition. University of British Columbia, Dept. of Oceanogr. Rep. 38, 183 pp.

McComas, C. H., and F. P. Bretherton, 1977: Resonant interaction of oceanic internal waves. *J. Geophys. Res.*, **82,** 1397–1411.

——, and P. Müller, 1981: Time scales of resonant interactions among oceanic internal waves. *J. Phys. Oceanogr.*, **11,** 139–147.

Mooers, C. N. K., 1973: A technique for the cross spectrum analysis of pairs of complex-valued time series, with emphasis on the

properties of polarized components and rotational invariants. *Deep-Sea Res.*, **20,** 1129–1141.

——, 1975: Several effects of a baroclinic current on the cross-stream propagation of inertial-internal waves. *Geophys. Fluid Dyn.*, **6,** 245–275.

Müller, P., 1976: On the diffusion of momentum and mass by internal gravity waves. *J. Fluid Mech.*, **77,** 789–823.

Munk, W., 1981: Internal waves and small scale processes. *Evolution of Physical Oceanography,* B. A. Warren and C. Wunsch, Eds., The MIT Press, 623 pp.

Niiler, P. P., 1982: "FRONTS-80"—a study of the North Pacific Subtropical Front. *Nav. Res. Rev.*, **34,** 41–50.

Paldor, N., 1983: Stable and unstable modes of surface fronts. *Geophys. Astro Phys. Fluid Dyn.*, **24,** 299–326.

Paulson, C. A., R. J. Baumann, L. M. deWitt, T. J. Spoering and J. D. Wagner, 1980: Towed thermistor chain observations in FRONTS '80. Oregon State University Data Rep. 85, Ref. 80-18, 183 pp.

Perkins, H., 1976: Observed effect of an eddy on inertial oscillations. *Deep-Sea Res.*, **23,** 1037–1042.

Pollard, R. T., 1980: Properties of near-surface inertial oscillations. *J. Phys. Oceanogr.*, **10,** 385–398.

——, and R. C. Millard, Jr., 1970: Comparison between observed and simulated wind-generated inertial oscillations. *Deep-Sea Res.*, **17,** 813–821.

Roden, G. I., 1975: On North Pacific temperature, salinity, sound velocity and density fronts and their relation to the wind and energy-flux fields. *J. Phys. Oceanogr.*, **5,** 557–571.

——, 1981: Mesoscale thermohaline, sound velocity and baroclinic flow structure of the Pacific Subtropical Front during the winter of 1980. *J. Phys. Oceanogr.*, **11,** 658–675.

——, and Paskausky, D. F., 1978: Estimation of rates of frontogenesis and frontolysis in the North Pacific Ocean using satellite and surface meteorological data from January 1977. *J. Geophys. Res.*, **83,** 4545–4550.

Rossby, C.-G., 1938: On the mutual adjustment of pressure and velocity distributions in certain simple current systems, II. *J. Mar. Res.*, **1,** 239–263.

Ruddick, B. R., and T. M. Joyce, 1979: Observations of interaction between the internal wave field and low-frequency flows in the North Atlantic. *J. Phys. Oceanogr.*, **9,** 498–517.

Sanford, T. B., 1985: The spatial structure of internal waves. (Unpublished manuscript).

——, R. G. Drever and J. H. Dunlap, 1978: A velocity profiler based on the principles of geomagnetic induction. *Deep-Sea Res.*, **25,** 183–210.

Simpson, J. H., C. M. Allen and N. C. G. Morris, 1978: Fronts on the continental shelf. *J. Geophys. Res.*, **83,** 4607–4614.

Tang, C. L., 1979: Inertial waves in the Gulf of St. Lawrence: A study of geostrophic adjustment. *Atmos.-Ocean,* **17,** 135–156.

Thomson, R. E., and W. S. Huggett, 1981: Wind-driven inertial oscillations of large spatial coherence. *Atmos.-Ocean,* **19,** 281–306.

Van Woert, M., 1982: The subtropical front: Satellite observations during FRONTS 80. *J. Geophys. Res.*, **87,** 9523–9536.

Veronis, G., 1956: Partition of energy between geostrophic and non-geostrophic oceanic motions. *Deep-Sea Res.*, **3,** 157–177.

Webster, F., 1968: Observations of inertial-period motions in the deep sea. *Rev. Geophys.*, **6,** 473–490.

Weller, R. A., 1982: The relation of near-inertial motions observed in the mixed-layer during the JASIN (1978) experiment to the local wind stress and to the quasigeostrophic flow field. *J. Phys. Oceanogr.*, **12,** 1122–1136.